EPJ manuscript No.
(will be inserted by the editor)

Nonlinear dynamics of triple quantum dot molecules in a cavity: multi-stability of three types of cavity solitons

M. Eslami[1a] and G.-L. Oppo[2]

[1] Department of Physics, University of Guilan, P.O. Box 41335-1914 Rasht, Iran
[2] Department of Physics, University of Strathclyde, Glasgow, G4 0NG, Scotland, EU

Received: date / Revised version: date

Abstract. By numerical simulation of a cavity filled with triple quantum dot molecules under tunneling induced transparency, we show that various regimes of existence of different kinds of cavity solitons are possible. Forming in overlapping regions of a multistable parameter space, cavity solitons in this system exhibit different dynamical behaviors: stationary on a flat background when there is only one cavity soliton branch, oscillating when two cavity soliton branches coexist, and stationary-rambling on a honeycomb background arising from simultaneous presence of a stable pattern and a cavity soliton branch. In particular, we show that three different types of dissipative localized structures can be excited in multistable regions where material coherence is high due to light-matter interaction processes.

PACS. XX.XX.XX No PACS code given

1 Introduction

Theoretical and experimental studies on nonlinear optical cavities have been the focus of many researchers for almost half a century. The motivation arises from diverse application prospects as well as interesting nonlinear cavity physics. These areas include all-optical storage and operations [1–6], photonic tools [7–13], pattern formation and self-organization [14–17], dissipative solitons [18–21], vortices [22–25] and extreme events [17,25–28].
With the introduction of quantum coherent phenomena a promising window has been opened in the realization of schemes required for efficient quantum information systems, coherent control protocols and light-matter interaction routes [29]. Electromagnetically induced transparency (EIT) in atomic systems and its solid state counterpart, tunnelling induced transparency (TIT), have shown to be effective multi-level processes in increasing material coherence and generating large nonlinearities leading to multistability, coexistence and competition of solutions [28,30,31]. The nonlinear scenario is more complex when spatio-temporal instabilities destabilize the competing attracting sets and multiple bifurcations affect the number and evolution of the solutions. In bistable cavities, bright cavity solitons (CSs) are generally formed in regions of coexistence of a low-intensity stable solution and a higher intensity solution affected by modulation (Turing) instability [32]. Recenly, Hansson and Wabnitz, going beyond Lugiato-Lefever equation (LLE) and mean-field approximation, numerically observed two different stable CSs corresponding to regular LLE CS and an excited state CS labeled as *super CS* [33]. The term *super* reflects the fact that the excited state CSs are much narrower than the regular LLE CSs which then can find interesting applications in frequency combs. Such localized structures were later experimentally verified in a passive Kerr resonator in the regime of continuous wave tristability where the presence of more than two coexistent continuous wave solutions can be associated with a different CS state [34]. Coexistence of two types of CSs due to overlapping resonances was also reported in ring resonators in [35] and for polariton solitons in microcavity wires [58].
Moreover, coexistence of multiple nonlinear states in a cavity can lead to even more exotic formations if one or more of these states are affected by temporal or spatial instabilities. For example, stable CSs atop a temporally oscillating spatially homogeneous background due to Hopf instability have been reported in semiconductor systems [37,38]. On the other hand, localized states on top of pattern backgrounds were first found in liquid-crystal light valves in a diffractive configuration of an optical system in [39] and later experimentally in [40] (see also [41]). CSs forming atop a spatially modulated background due to the Turing instability have also been reported recently in [34] where stable coexistence of temporal Kerr CSs and extended modulation instability is discussed and claimed to be the first observation of its kind. An interesting observation made there was the extension of CS branch of the first resonance into the region of cw bistability of the second resonance when the driving was sufficiently strong. They showed that in this regime, the intracavity field is

[a] e-mail: meslami@guilan.ac.ir

composed of two different CS states both sitting on top of the lower state cw solution of the second resonance with distinct duration, peak and power [34]
In this paper, we generalize these discussions to the transverse spatio-temporal dynamics of a nonlinear cavity filled with quantum dot molecules under TIT. We focus in particular on the coexistent multiple nonlinear states and overlapping Turing instability domains. We show that the nonlinear behaviour of such a model is rich enough to exhibit different regimes of existence for CSs when the system is either in bistable or tristable state. Bistability and tristability refer to the continuous wave solutions without spatial coupling (i.e. when neglecting diffraction). We introduce *different types of* CSs corresponding to isolated cells of a stable pattern solution (due to Turing instability) either belonging to the intermediate intensity branch (first type CS) or that of a coexistent higher intensity branch (second type CS) sitting on a low intensity homogeneous state in a tristable solution space. The third type of CSs is found when the control parameter is further increased and larger switching pulses are used to excite CSs of much higher intensities (at least 3 times larger than the first two levels). We label these intense CSs as *high-level* CSs to distinguish them from those of ordinary intensity. Our *high-level* CSs (the third type of CS) are different from those of multiple-state purely temporal configuration in [34] where a CS branch of first resonance is extended into the bistable region of the second resonance giving rise to a state of coexistent CSs of two neighboring resonances. These can be regarded similar to the first and second types of CSs in our three type localized solutions of a transverse spatio-temporal dynamics where an upper branch emerges above those of intermediate and low intensity solutions when increasing the control parameter. To our knowledge, there has been no report of *high-level* CSs of peak intensities much higher than those of ordinary intensity (first and second kind CSs) and yet sharing the same low intensity homogeneous background.
After introducing the mean-field model and calculations of the associated nonlinear term in section 2, we turn our attention to its multistability feature and domains of spatial instability in section 3. Cavity soliton branches and their properties are then discussed in sections 4, 5, 6, and 7 respectively including stationary CSs over a flat background, oscillating CSs on a steady background, stationary and rambling CSs over a honeycomb background, and high-level CSs. Final remarks and conclusions appear in section 8.

2 The model

A ring cavity filled with triple quantum dot molecules is considered where the dots in individual molecules are coupled by electric gates as shown in Fig. 1. Realization of EIT and coherent population trapping (CPT) in atomic systems require laser beams for coupling appropriate energy levels; however, the same purpose is served by voltage gates in quantum dot molecules which can, in effect, control electrons' tunneling rates between different

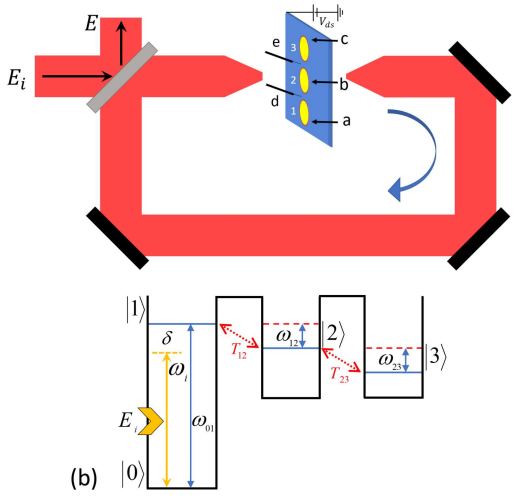

Fig. 1. (Color online) (a) Cavity configuration for a typical triple quantum dot molecule with an external injection and tunneling indexes controlled by gate voltages. Labels a, b and c refer to the bottom, center and top dot plunger gates, respectively and gates labeled d and e are used to tune the tunnel barriers between the bottom and center dots and between the center and top dots, respectively. A drain-source bias V_{ds} is also depicted. For more details regarding the fabrication and material see [42–44]. Typical specifications are: active region thickness around 200 nm, overall thickness including DFB mirrors around 0.5 μm, active emission area around 0.023 cm^2, and emission wavelength around 630 nm. (b) Energy-level structure for the dots in the molecule.

energy states. Such conditions can be tuned to achieve tunneling induced transparency for solid state devices as compared to electromagnetically induced transparency in atomic media. Recent progress on fabrication techniques, experiments and application prospects with triple quantum dot structures can be found in [42]. Although the focus in this paper is about solid-state quantum dot devices, we note that the model and results apply equally well to three level atomic gases in optical resonators [45] and to silica based optical microcavities [46].
Cavity configuration can be described by a single mean-field equation [28,47–51]:

$$\partial_t E = E_i - [(1 + i\theta) + i\Sigma\chi(E)]\, E + i\nabla^2 E, \qquad (1)$$

where E and E_i are respectively the slowly varying amplitude of the electric field and the injected pump field both scaled to the square root of the saturation intensity of the first quantum dot transition. The injected pump E_i has a frequency ω_i close to that of the transition $|0\rangle \rightarrow |1\rangle$ which couples the ground state $|0\rangle$ with the exciton state $|1\rangle$ (a pair of electron and hole bound in the first dot). The electron tunneling, on the other hand, couples the exciton $|1\rangle$ with the indirect exciton state $|2\rangle$ (one hole in the first dot with an electron in the second dot) and also with the indirect exciton state $|3\rangle$. The detuning term θ is the frequency difference between the cavity resonance and ω_i normalized to the inverse of the photon lifetime. The

diffraction term is given by the Laplacian operator in two transverse dimensions and time is normalized to the photon life time in the cavity. Σ is the cooperative parameter directly proportional to the number density of quantum dot molecules N through

$$\Sigma = \frac{N\mu_{01}^2 kL}{\hbar\Gamma\epsilon_0 T}\,, \tag{2}$$

where μ_{01} is the transition dipole moment, k the wave number of the cavity field, L the length of the cavity, Γ the linewidth, ϵ_0 the permittivity of free space, and T is the cavity mirror transmittivity. $\chi(E)$ is the complex susceptibility which contains all the medium-related details due to the off-diagonal density matrix elements when multiplied by the field amplitude E. We note that non-interacting situation among individual quantum dot molecules inside the cavity is considered in the formalism for simplicity.

The Hamiltonian of the system for the energy level configuration shown in Fig. 1(b) can be written as follows:

$$H = H_0 + H_I + H_T, \tag{3}$$

where the unperturbed, interaction and tunneling Hamiltonian terms respectively are :

$$H_0 = \hbar\sum_{j=0}^{3}\omega_j|j\rangle\langle j|, \tag{4}$$

$$H_I = \frac{1}{2}E_i\mu_{01}|0\rangle\langle 1|e^{(ik.z-i\omega_i t)} + H.\,C., \tag{5}$$

$$H_T = T_{12}|2\rangle\langle 1| + T_{23}|3\rangle\langle 2| + H.\,C. \tag{6}$$

where $H.\,C.$ stands for Hermitian Conjugate. In the Hamiltonian terms above, j represents the respective energy level, z is the longitudinal coordinate, T_{12} and T_{23} denote the electron tunneling matrix elements for $|1\rangle \to |2\rangle$ and $|2\rangle \to |3\rangle$ transitions, respectively. It should be noted that in the effective time scale here hole tunneling can be neglected.

The dynamics of the medium variables is described by the master equation of motion for density matrix:

$$\dot{\rho} = -\frac{i}{\hbar}[H, \rho]. \tag{7}$$

Under the rotating-wave approximation, equations of motion for density matrix elements are obtained as follows:

$$\dot{\rho}_{01} = iE + (i\delta - \gamma_{01})\rho_{01} + iT_{12}\rho_{02}, \tag{8}$$

$$\dot{\rho}_{02} = \{i(\delta - \omega_{12}) - \gamma_{20}\}\rho_{02} - iE\rho_{12} + iT_{12}\rho_{01} + iT_{23}\rho_{03}, \tag{9}$$

$$\dot{\rho}_{03} = \{i(\delta - \omega_{12} - \omega_{23}) - \gamma_{30}\}\rho_{03} - iE\rho_{13} + iT_{23}\rho_{02}, \tag{10}$$

$$\dot{\rho}_{12} = -(i\omega_{12} + \gamma_{12})\rho_{12} - iE^*\rho_{02} + iT_{23}\rho_{13}, \tag{11}$$

$$\dot{\rho}_{23} = -(i\omega_{23} + \gamma_{23})\rho_{23} - iT_{12}\rho_{13}, \tag{12}$$

$$\dot{\rho}_{13} = -(i\omega_{13} + \gamma_{13})\rho_{13} - iE^*\rho_{03} - iT_{12}\rho_{23} + iT_{23}\rho_{12} \tag{13}$$

where δ is the frequency mismatch between the injected field and the $|0\rangle \to |1\rangle$ transition which is normalized to the linewidth of the quantum dot transition, here considered to be positive for a self-focusing nonlinearity. ω_{12} is the frequency difference between levels $|1\rangle$ and $|2\rangle$ and ω_{23} is that of $|2\rangle$ and $|3\rangle$. Both of the level separations are managed by electric gates which give control over the occupation of levels $|2\rangle$ and $|3\rangle$ [52]. The relaxation rate γ_{01} is taken as unity while all others are $10^{-3}\gamma_{01}$ [53,54]. We note that such an analysis is relevant for quantum-confined semiconductor systems where excitonic transitions are dominant. These are more pronounced in quantum dots (3D carrier confinement) than in quantum wells (1D carrier confinement). Similar calculations can be found, for example, in [52,53,55,56] for variety of quantum-confined structures.

These coupled equations are solved for ρ_{01} under steady state conditions along with an additional condition that the sum of the probabilities of occupancy of the levels is equal to one and can be written in a compact form as:

$$\rho_{01} = E\frac{A + iB}{C + iD}, \tag{14}$$

where A, B, C, and D are all functions of $(\delta, \omega_{ij}, T_{12}, T_{23}$ and $|E|^2)$. This expression is then substituted in Eq. (1) according to $\chi(E) = \rho_{01}/E$. Real and imaginary parts of the derived nonlinearity identify a large dispersion curve slope along with a vanishing absorption around $\delta = 0.37$ [28].

3 Multistability of homogeneous states and multistable patterns

Multistability in this system is achieved for homogeneous steady states ($\partial_t = 0$ and $\nabla^2 = 0$ in Eq. (1)) when population in level $|2\rangle$ is increased via the control parameter ω_{12} (or equivalently the gate voltage) allowing for more absorption in the transition $|0\rangle \to |1\rangle$. By increasing the control parameter value at the fixed stationary intensity $|E_s|^2 = 0.2$, monostability changes into bistability at $\omega_{12} = 0.25$ beyond which a lower intensity branch develops in simultaneous presence of the already established higher intensity solution. A second critical point is found at $\omega_{12} = 0.38$ where an even lower intensity branch appears leading to tristability with the two previously described branches. The system then returns to a bistable state by removing the branch of the lowest intensity when the control parameter is further increased to $\omega_{12} = 0.41$. At $\omega_{12} = 0.51$, the solutions with the lowest intensity is recovered (enduring for all control parameter values larger than this critical point) and the tristable state emerges once more. When the control parameter value crosses $\omega_{12} = 0.59$, the highest intensity branch disappears and bistability dominates again between the moderate intensity solutions and those of the lowest intensity. The branch of highest intensity develops again at the critical value of $\omega_{12} = 0.63$ and tristability occurs for the third time lasting until $\omega_{12} = 1.54$ after which

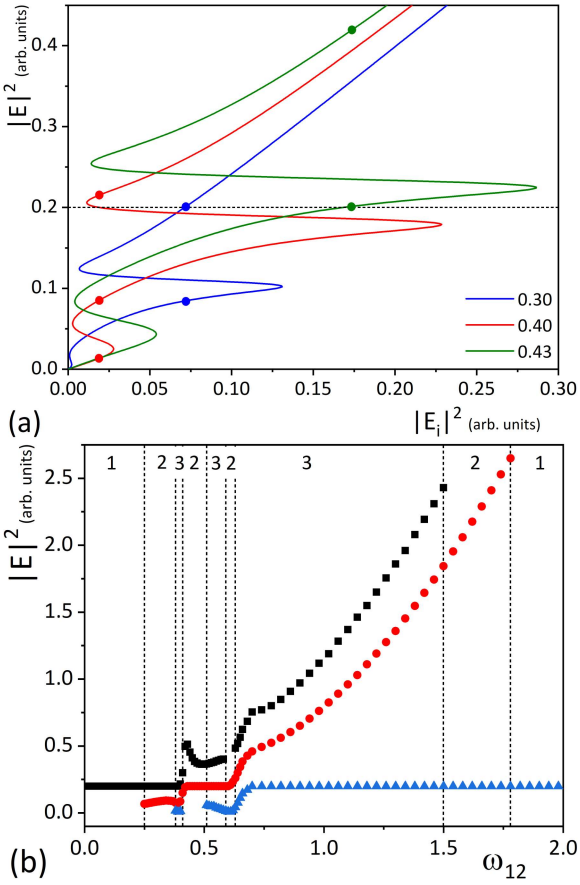

Fig. 2. (Color online) (a) Mono-, bi-, and tri-bistable states of the system when the control parameter value ω_{12} is increased from 0.30 to 0.40 and 0.43. The available outputs for the fixed stationary intensity $|E_s|^2 = 0.2$ are depicted by circles. (b) Multistable solution space for different values of the control parameter. Monostable, bistable and tristable regions are marked respectively by numbers 1, 2, 3. Other parameter values are: $\Sigma = 1, T_A = 0.1, T_B = 0.01, \omega_{23} = 0.3, \delta = 0.3$, and $\theta = -0.5$.

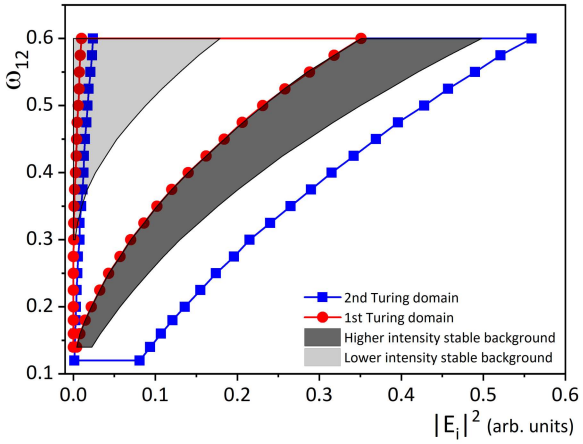

Fig. 3. (Color online) Overlapping stable and unstable domains in $\omega_{12} - |E_i|^2$ parameter space. Stable homogeneous branches (light and dark gray) coexist with Turing domains of different critical wave-vectors (blue squares affecting the upper branch and red circles the middle one). Parameter values are the same as in Fig. 2.

bistability and then monostability (at $\omega_{12} = 1.82$) dominate since the branches of highest and moderate intensity solutions vanish respectively. For higher control parameter values monostability is the only feature of the system. These transitions and the coexistent states are shown in Fig. 2(a) and (b).

The linear stability analysis of the homogeneous stationary solutions, i.e. the response of the system to small fluctuations around the steady states, provides the most unstable spatial wave-vectors which rule the periodicity of the emerging pattern in a mechanism typical of Turing pattern formation [32,51,57]. For the parameter values capable of a multistable behaviour, separate Turing domains and branches have been reported for our system leading to conditions for pattern competition and optical turbulence with the possibility of triggering 2D rogue waves [28]. Coexistence of Turing unstable branches at higher intensities with a low-intensity stable homogeneous branch is a generic feature of this system and is shown in Fig. 3 in the parameter space $(|E_i|^2, \omega_{12})$. We observe that depending on the value of the control parameter different branches in the multistability curve experience Turing instability with a different critical wave-vector K_c: the region delimited by squares shows the instability for small K_c domain and that by circles for large K_c domain. In addition to the fact that these separate Turing domains coexist for certain range of parameter values (see the overlapping region of the areas delimited by squares and circles in in Fig. 3), they also coexist with stable backgrounds illustrated by light and dark gray areas in the figure. Specifically, the Turing domain of small K_c coexists in part with both the lower intensity and higher intensity stable backgrounds. However, the Turing domain of large K_c is only coexistent with the lower intensity stable background. These are also evident in Fig. 4(a) and (c) and have different consequences in the nonlinear dynamics of the cavity.

In a typical bistable condition and in presence of self-focusing nonlinearity, the lower intensity stable homogeneous solution can surround one cell of the higher intensity pattern formed as a result of Turing instability thus providing the necessary conditions for the formation or excitation of localized structures known as cavity solitons. Here, we numerically check the existence and properties of CSs in four regimes: i) CSs on a flat (homogeneous) background, ii) temporally oscillating CSs on a stationary background, iii) CSs on a honeycomb background and iv) high-level CSs with peak intensities much higher than the stable or unstable homogeneous solutions. Numerical simulation of the system is carried out through the standard split-step method separating and solving time derivative and diffraction terms respectively by Runge-Kutta and Fast Fourier Transform methods. We have used grid sizes

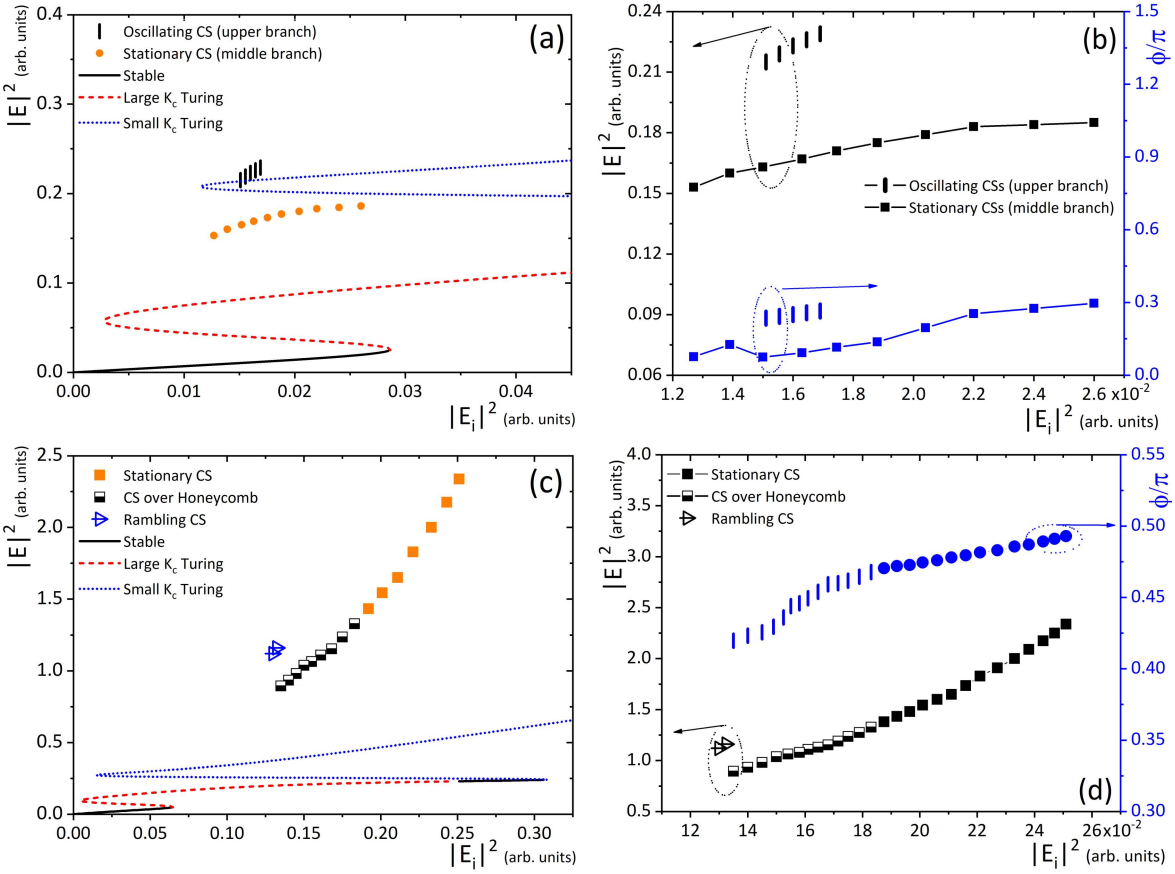

Fig. 4. (Color online) (a) Multistability curve and the CSs belonging to middle and upper branches sharing the same low intensity stable background for $\omega_{12} = 0.402$. (b) Intensity and phase values of these CSs versus pump value. For oscillating CSs we have considered their maximum values in intensity and phase. (c) Multistability curve and the CSs belonging to the middle and upper branches where the middle branch serves as the low-intensity background for the CSs. The control parameter value is $\omega_{12} = 0.4675$. (d) Intensity and phase values of these CSs versus pump value. K_c stands for the critical wave-vector related to the Turing instability domains and the parameter values are the same as in Fig. 2.

up to 128×128 lattice sites and guaranteed that the results are fully reproducible.

4 Stationary CSs on a flat background

We have performed direct numerical simulations of the dynamical equations as described in [28,30,31] to find CS states over broad ranges of parameter space. Stable CS states have been tested to random perturbations. Two regimes of stationary CSs are accessible in different sections of the multistability curves depending on the values of the control parameter. The first regime of existence of stationary CSs is found in the interval $|E_i|^2 = (1.44 - 2.60) \times 10^{-2}$ corresponding to localized structures connecting individual cells of the pattern solution of intermediate intensity located on the middle branch, and the homogeneous background located on the low-intensity branch. While the first regime is specific to the section on the left of the multistability curves in Fig. 2 where tristability is present, the second regime of existence for stationary CSs can be achieved on the right hand side of the same figure within the bistable situation. In the interval $|E_i|^2 = (19 - 25.5) \times 10^{-2}$, stationary CSs are observed to form due to coexistence of the intermediate intensity stable homogeneous solution located on the rightmost part of the middle branch and pattern solution of higher intensity belonging to the uppermost branch. In both cases, CSs are created on a flat background provided either by the lowest intensity branch or the intermediate intensity branch with typical features of regular CSs. Fig. 4(a) depicts the CSs belonging to the first regime discussed above while Fig. 4(c) illustrates those of the second regime along with the curves associated with the stationary solutions. The intensity and phase values of these CSs are shown in detail in Fig. 4(b) and (d).

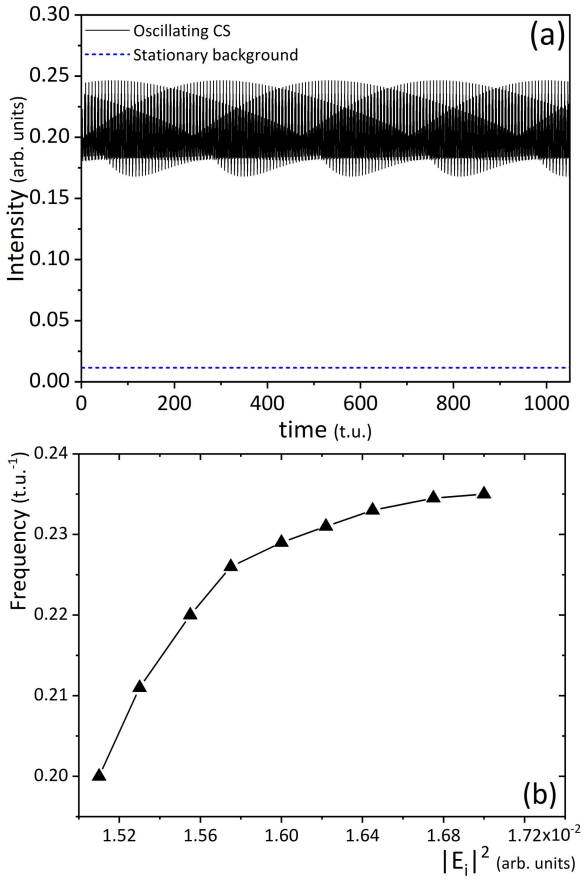

Fig. 5. (a) Time evolution of intensities of an oscillating CS and its stationary background for $|E_i|^2 = 1.64 \times 10^{-2}$ and $\omega_{12} = 0.399$. (b) Frequency of CS intensity oscillations versus pump intensity. Note that by increasing ω_{12} stationary intensity falls onto the middle branch experiencing only one unstable domain and thus CSs become stationary in their intensity. Parameter values are the same as in Fig. 2.

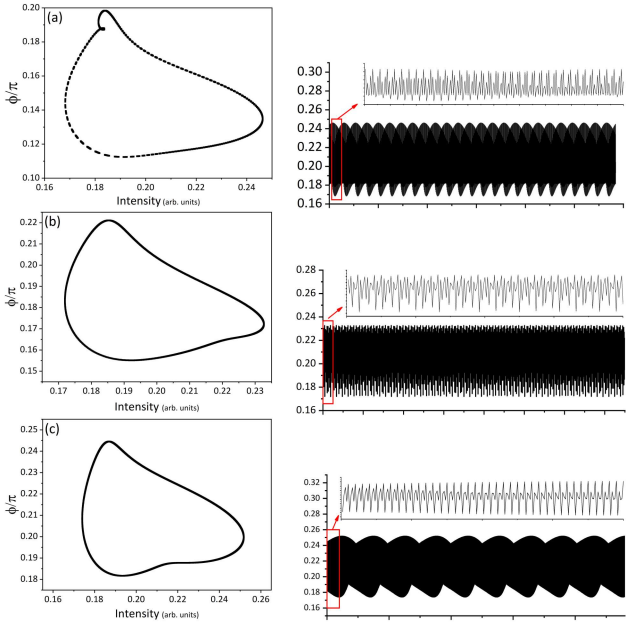

Fig. 6. Limit-cycle trajectories for oscillating CSs (left panels) and their peak-intensity time evolution (right panels) for (a) $\omega_{12} = 0.399$ and $|E_i|^2 = 1.64 \times 10^{-2}$, (b) $\omega_{12} = 0.400$ and $|E_i|^2 = 1.88 \times 10^{-2}$, and (c) $\omega_{12} = 0.401$ and $|E_i|^2 = 2.2 \times 10^{-2}$. The horizontal axes in the plots of the right panels represents time from zero to 20000 time units. Other parameter values are the same as in Fig. 2.

5 Oscillating CSs on a stationary background

As it is seen from figures 4(a) and (b), for smaller values of the control parameter ω_{12} the fixed stationary intensity at 0.2 lies entirely on the uppermost branch coexistent with two lower intensity branches, one of which is modulationally unstable. This gives rise to oscillations in the intensity and phase of the CSs excited on the upper branch in the range $|E_i|^2 = (1.5-1.7)\times 10^{-2}$. We note that these CSs sit on a homogeneous stationary background belonging to the lowest intensity branch. The intensity versus time plots for an oscillating CS and its homogeneous stationary background are shown in Fig. 5(a) along with the frequency of oscillations throughout their existence range in Fig. 5(b). The reason behind this phenomenon is the fact that although a very low-intensity stable homogeneous state exists, these CSs are affected by the Turing instability of the middle branch having a different critical wave-vector and a relatively lower intensity than those of the uppermost branch. In a special case where the two instability domains (Turing domains affecting the uppermost and middle branches) have comparable strength, pattern competition is observed leading to 2D optical turbulence and generation of rogue waves in the absence of any stable homogeneous solution [28]. In terms of the injected intensity $|E_i|^2$, these oscillating CSs of the uppermost branch are bistable with stationary CSs of the middle branch both sharing the same stable homogeneous background of the lowest intensity.

To further characterise the dynamics of these oscillating CSs, we show their limit cycles (peak intensity, phase) along with their peak-intensity time traces in Fig. 6. These plots correspond to three parameter values of $\omega_{12} = 0.399$, 0.400, 0.401 and $|E_i|^2 = 1.64 \times 10^{-2}$, 1.88×10^{-2}, 2.2×10^{-2}, respectively, to illustrate the extent of the intensity variations (oscillation amplitudes) and signature bound phase behavior for these CSs.

6 CSs on a honeycomb background

The third regime is associated with the CSs belonging to the rightmost bistable part of the multistability curve with a stable background which has the intensity of the middle branch, as it can be seen from Fig. 4(c). By increasing the control parameter ω_{12} from 0.4275 to 0.4675 it is observed that the extent of the stable section serving as the

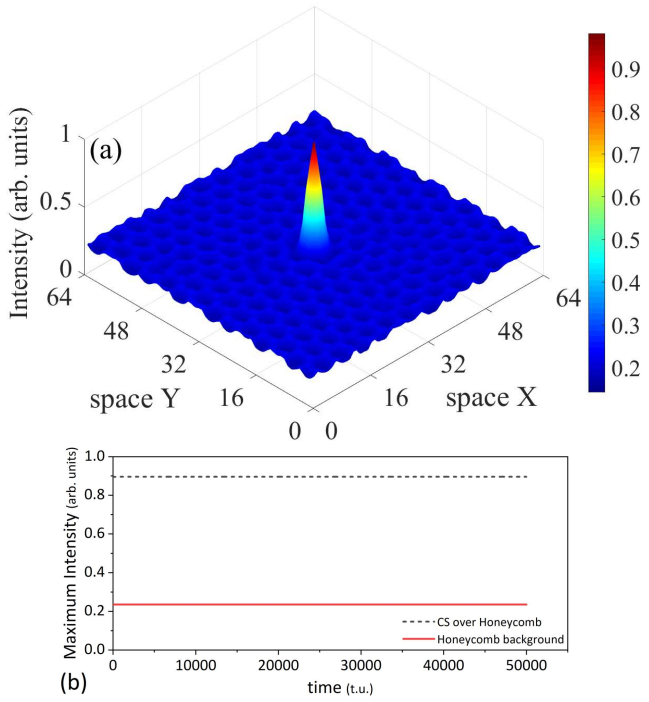

Fig. 7. (Color online) (a) 3D plot of the output intensity showing the honeycomb pattern serving as the less intense background for the CS ($|E_i|^2 = 0.145$ and $\omega_{12} = 0.46$) and (b) the intensity versus time for the CS and its honeycomb background. Other parameter values are the same as in Fig. 2.

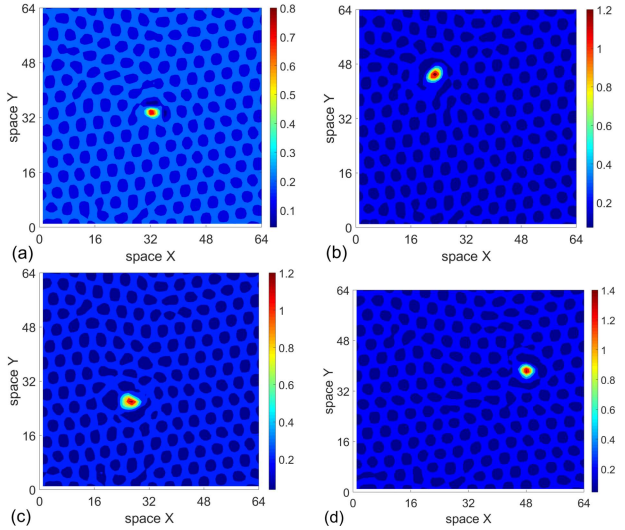

Fig. 8. (Color online) Snapshots of the output intensity which shows the drift of the CS along the side of the underlying honeycomb background. Time in the snapshots progresses as (a) t_0, (b) $t = t_0 + 150$, (c) $t = t_0 + 450$ and (d) $t = t_0 + 850$ in terms of time units. $|E_i|^2 = 0.132$, $\omega_{12} = 0.4675$ and other parameter values are the same as in Fig. 2.

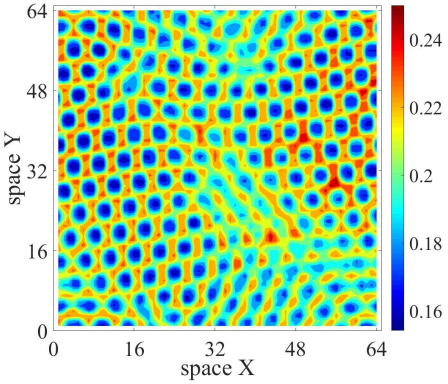

Fig. 9. (Color online) The honeycomb pattern reconstructed by the rambling CS when average is taken from output intensity over 3500 time units. $\omega_{12} = 0.4675$ and other parameter values are the same as in Fig. 2.

background for these CSs shrinks and the Turing domain of the middle branch sets in. This process leaves the stable CSs with a modulation unstable background which in turn gives them interesting new features. As a result, CSs first loose their stable homogeneous (flat) background to a honeycomb pattern which traps them in its intensity maxima and then, by further increasing ω_{12} that gives more stability to the honeycomb solution, the trapped CSs start to ramble along the sides of the honeycomb pattern where the intensities are the highest. In Fig. 4(d), intensity and phase variations of these CSs with the pump intensity are depicted.

In Fig. 7(a) a stable CS over honeycomb pattern state is shown for $|E_i|^2 = 0.145$ and $\omega_{12} = 0.46$. Also depicted is the comparison of the CS intensity and the honeycomb background intensity (at its maxima) through time in Fig. 7(b) which shows stationary values for both the CS and the honeycomb background intensities. When the control parameter values are increased, we observe faster relaxations to the stable honeycomb background. At the same time, the original CS starts moving around the honeycomb structure with no preferred direction. The snapshots of Fig. 8 show the rambling CS over a honeycomb pattern for increased control parameter values of $|E_i|^2 = 0.132$ and $\omega_{12} = 0.4675$ at different times. Fig. 9 in particular shows the average output intensity over 3500 t. u. confirming that the CS moves along the sides of the underlying honeycomb pattern.

Since the CSs of different regimes mentioned above belong to different states of the system having coexistent branches of different intensities and critical wave-vectors for Turing instabilities, we expect them to have distinct features. For instance, in Fig. 10(a) it is seen that CSs belonging to the bistable state located on the rightmost part of the multistability curves exhibit a full width at half maximum (FWHM) value that is almost two times that of CSs forming in the leftmost section of the multistability curves. Moreover, due to the different intensities of the involved background states, they are observed to have dif-

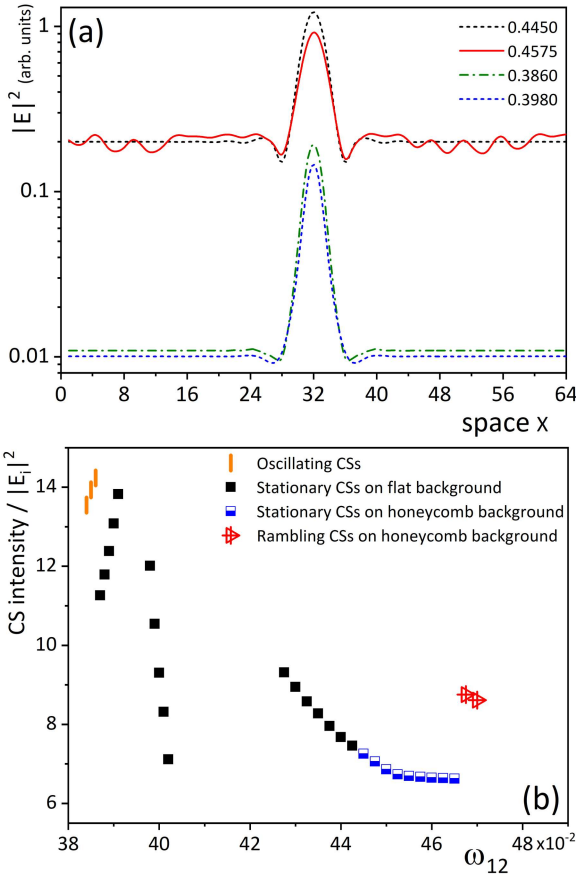

Fig. 10. (Color online) (a) Intensity profiles along the horizontal axis for stationary CSs and CSs over honeycomb patterns at $\omega_{12} = 0.4450 (|E_i|^2 = 0.183)$ and $\omega_{12} = 0.4575 (|E_i|^2 = 0.15)$, and those for stationary and oscillating CSs at $\omega_{12} = 0.398 (|E_i|^2 = 1.44 \times 10^{-2})$ and $\omega_{12} = 0.386 (|E_i|^2 = 1.51 \times 10^{-2})$, respectively. (b) Efficiency value (the ratio of CS intensity to that of pump) in terms of the control parameter ω_{12}. The discontinuities in the left part of the figure are due to the replacement of the involved Turing branches in the formation of CSs and the Turing destabilization of the lower intensity background in the right part. Parameter values are the same as in Fig. 2.

ferent contrast (CS intensity/background intensity) and efficiency (CS intensity/pump intensity) values. For the CSs forming in the bistable and tristable states of the leftmost part of the multistability curves the contrast value varies between 15 and 22 while the range is only between 5 and 10 for the CSs of the bistable state in the rightmost section of the multistability curve. For the efficiency parameter, Fig. 10(b) shows that it effectively depends on the location of the modulation unstable branch since the low intensity homogeneous solutions change their intensity very slightly while the Turing-affected branch involved in formation of the CSs can shift from the highest intensity branch to the intermediate intensity branch when changing the control parameter. This trend is very less dramatic

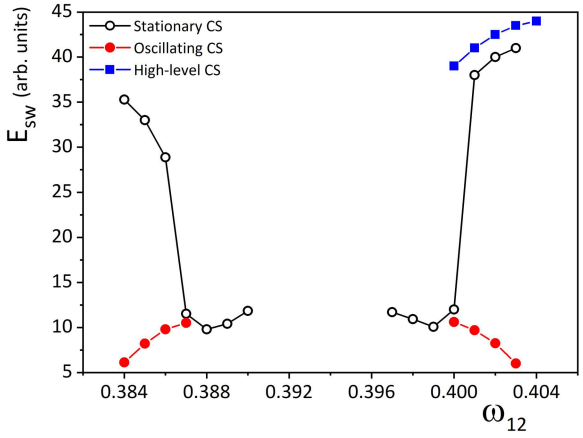

Fig. 11. (Color online) Switching energies involved in exciting stationary (black circles), oscillating (red filled circles) and *high-level* cavity solitons (blue squares) in terms of the control parameter for the tristable region. Parameter values are the same as in Fig. 2.

for the CSs belonging to the bistable state of the rightmost part of the multistability curve since replacement of the Turing-affected branch is not involved.
We conclude this section by stressing that all CS types discussed here are stable as verified by long simulation times of the model and robustness to perturbations. This stability extends the results of [58] where CSs of first and second type have been found to be stable only when the system is in a two-state situation. In our case, instead, stability of all the CS types reported here is robust regardless of the number of coexistent solutions.

7 Switching of Bistable and multi-level CSs

In this section we turn our attention to the switching of multi-state CSs of the tristable region found at the leftmost section of the multistability curves, see Fig. 4(a). Excitation of stationary CSs on a flat background or oscillating CSs is possible at the same control parameter value by tuning the switching pulse energy. Various mechanisms of CS switching have been reported for a variety of devices [59–63]. Here, however, we only use the coherent switching method through a Gaussian address pulse in the form below:

$$E_{sw}(x_0, y_0) = E_0 e^{\frac{(x-x_0)^2+(y-y_0)^2}{w^2}}, \qquad (15)$$

where E_0 and w are the amplitude and width of the Gaussian address pulse respectively. (x, y) represent the transverse coordinates and (x_0, y_0) is where the address pulse falls onto. Note that this equation does not have a phase term meaning that it is taken to be in phase with the pump. We note, however, that the same pulse with a π phase difference with the pump would switch off the CS. To have a better quantitative comparison among separate

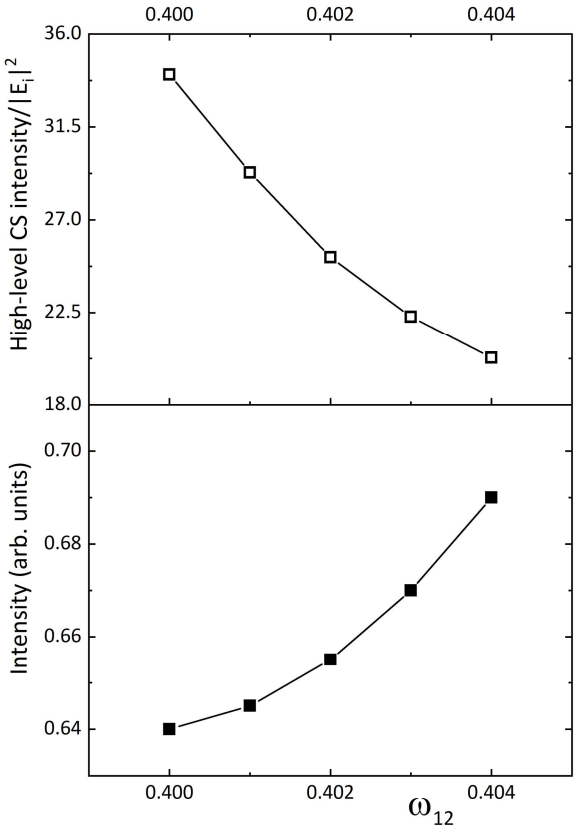

Fig. 12. (Color online) Intensity and efficiency values of high-level cavity solitons versus the control parameter. Parameter values are the same as in Fig. 2.

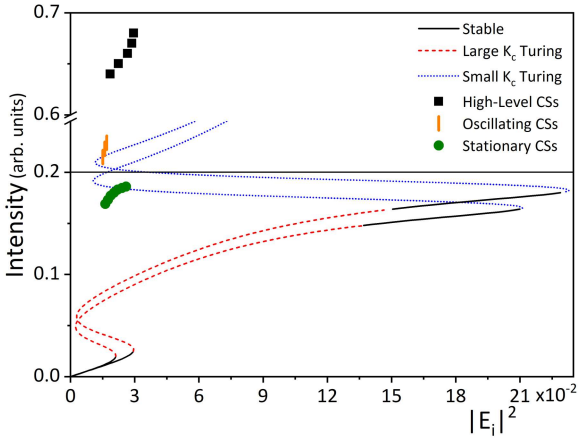

Fig. 13. (Color online) High-level CSs achievable for higher control parameter values for which the system is prepared on the middle branch for the fixed stationary intensity $|E_s|^2 = 0.2$, here $\omega_{12} = 0.404$. A less extended curve (all black with dash-dots) is also shown for comparison for which the system is prepared on the upper branch for the fixed stationary intensity of $|E_s|^2 = 0.2$ where high-level CSs are not supported, here $\omega_{12} = 0.384$. Parameter values are the same as in Fig. 2.

simulations, we use the scaled equation $E_{sw} = |E_0|^2 t_{inj}$ for the switching energy which provides a rough estimate of the energies involved in switching of CSs with different dynamical behaviour for the same control parameter value.

Fig. 11 shows the threshold energies required for switching different CSs. It is seen from the figure that oscillating CSs are excited by lower switching pulse energies compared to stationary CSs forming on a flat background at the same control parameter values. This is a relevant feature at both ends of the CS interval. It is important to note that by increasing the control parameter from $\omega_{12} = 0.384$ to $\omega_{12} = 0.397$ at a fixed stationary intensity of $|E_s|^2 = 0.2$, the system moves from the upper branch to the middle branch in the multistability curves. Switching energies E_{sw} shown on the left (right) part of Fig. 11 belong to CSs with peak intensities close to the upper (middle) branch. One can then conclude that oscillating CSs being bistable with stationary CSs experience intensity fluctuations only because they are affected by a Turing unstable solution that is coexistent with that which localizes them in presence of the lowest intensity flat background. They are found at both ends meaning that their existence and oscillating character are independent of the system having been prepared in the upper branch or on the middle branch with stationary intensity $|E_s|^2 = 0.2$. While bistable CSs exist both at the left and right ends of Fig. 11, there is a branch of switching energies E_{sw} that is only found at the right end and is above other branches in the interval $\omega_{12} = 0.4-0.404$. Switching pulses of these energies excite CSs with intensities much larger than those shown in Fig. 4 and featuring large efficiency values as shown in Fig. 12. To distinguish these CSs from those of ordinary intensity, we label them as *high-level* CSs. Although CSs that can be switched on at both ends of the figure have a flat background on the lowest intensity branch, *high-level* CSs are only achievable when the control parameter exceeds $\omega_{12} = 0.40$ at which the system moves from the uppermost branch affected by the smaller critical wave-vector Turing instability to the middle branch of larger Turing critical wave-vector for the fixed stationary intensity of $|E_s|^2 = 0.2$, as shown in Fig. 13. This explains why these *high-level* CSs require the initial state to be prepared in the Turing domain of larger critical wave-vector unlike similar tristable situations with smaller control parameter values where the system is initially prepared in the Turing domain of smaller K_c for $|E_s|^2 = 0.2$ and *high-level* CSs cannot be excited at all. A typical high-level CS configuration is shown in Fig. 14.

At difference from their temporal counterpart reported and named as *super cavity solitons* in [33,34] which are narrower, these CSs of nonlinear states come with a broad spatial width compared to ordinary CSs at the same control parameter value. This is consistent with the fact that these *high-level* CSs originate from transverse modes affected by instabilities of a different spatial wavelength corresponding to the larger critical wave-vector Turing

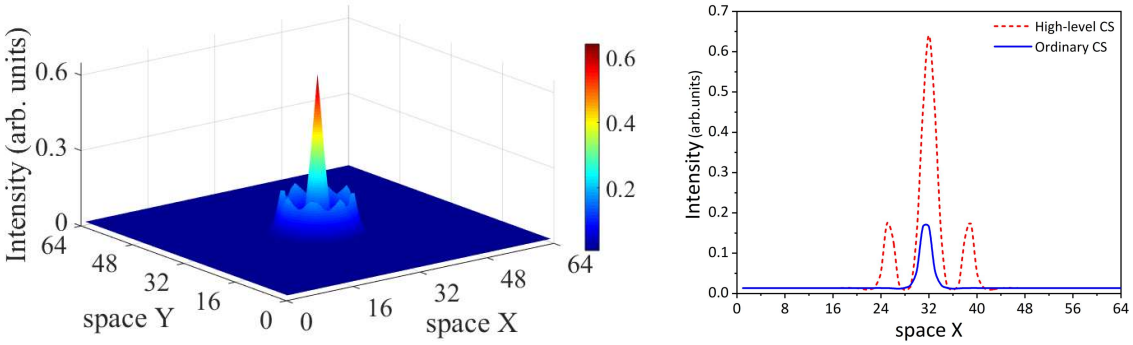

Fig. 14. (Color online) A high-level cavity soliton excited at $\omega_{12} = 0.4$ and its horizontal intensity profile compared with an ordinary CS excited at the same control parameter. Parameter values are the same as in Fig. 2.

domain. Multi-stability in our system is in fact induced not just by coexisting resonances but also by coexistent states of different spatial wavelength on the same resonance. The high-level CS is a hybrid soliton of multi-stable resonances and coexisting (not necessarily bistable) spatial wave-vectors. As it is shown in Fig. 14, these *high-level* CSs are 22 percent broader and 4 times more intense (on average) than their regular siblings. The black squares in Fig. 12 and Fig. 13 show that the high peak intensity of *high-level* CS persists for the full parameter region of their existence.

8 Conclusion

Since the introduction of quantum coherent phenomena such as electromagnetically induced transparency, many attempts have been made to investigate their interesting features with the aim of opening novel application prospects. However, it is the realization of those phenomena in solid state devices that can make them compatible with integrated photonics. Tunneling induced transparency, the solid state version of electromagnetically induced transparency, realized in triple quantum dot molecules with the benefit of controlled electronic transitions have made it possible to employ a combination of quantum and nonlinear optical features within the confinement of a cavity. Our work shows the ubiquity of cavity solitons in these devices that can be used as digital optical memories. Regimes of multi-stable cavity solitons allow for multi-state digital optical memories where the coding power of stored signals is greatly enhanced.

Here, the nonlinear dynamics of a cavity filled with triple quantum dot molecules is investigated numerically under the conditions of tunneling induced transparency. The large material coherence provided by quantum coherent phenomena generates multistate solution space. In such a configuration, simultaneous presence of spatial instabilities of different critical wave-vectors has already been shown to give rise to pattern competition and optical turbulence [28]. Here we have shown that the coexistence of a low-intensity homogeneous stable solution with branches affected by Turing instabilities prepares the system to form cavity solitons of three different types and with unique characteristics depending on the type of coexistent solutions. In particular, through dynamical simulations, we reported and found regimes of stability of regular, oscillating, bistable and *high-level* cavity solitons. The first two types of CSs being related to different branches of multistable stationary homogeneous solutions are the extension to the spatio-temporal regime of those predicted and verified in [33,34] for a purely temporal regime although without the introduction of Ikeda maps. *High-level* cavity solitons do not have a counterpart in previous studies of either spatial or temporal systems. They correspond to much more intense and broader dissipative localized structures than those expected by the simple intensity values of the multistable homogeneous solutions. *High-level* cavity solitons add to the rich landscape of complex localized and extended structures in nonlinear optical cavities and can offer the operator possible use of simultaneous and controllable pixel elements for encoding of optical information and smart optical memories.

Although the present study has focused on the spatio-temporal features of a three-level medium in a cavity in the presence of transverse diffraction, we expect many of these results to hold in the presence of longitudinal dispersion in both regimes of anomalous and normal dispersion. Fast time features and applications of the three types of cavity soltions identified in this work in ring resonators will be reported in future communications.

9 Acknowledgment

The authors would like to acknowledge the financial support of University of Guilan for this research under grant number 132656.

References

1. S. D. Smith, Optical Bistability: Towards the Optical Computer, Nature (London) **307**, 315 (1984).

2. G. S. McDonald and W. J. Firth, Spatial solitary-wave optical memory, J. Opt. Soc. Am. B **7**, 1328 (1990).
3. S. Barland, J. R. Tredicce, M. Brambilla, L. A. Lugiato, S.Balle, M. Giudici, T. Maggipinto, L. Spinelli, G. Tissoni, T.Knödl, M. Miller, and R. Jäger, Cavity solitons as pixels in semiconductor microcavities, Nature (London) **419**, 699 (2002).
4. M. Eslami and R. Kheradmand, All optical logic gates based on cavity solitons with nonlinear gain, Optical Review **19**, 242-246 (2012).
5. A. Jacobo, D. Gomila, M. A. Matías, and P. Colet, Logical operations with localized structures, New Journal of Physics **14**, 013040 (2012).
6. Q. Vinckier, F. Duport, A. Smerieri, K. Vandoorne, P. Bienstman, M. Haelterman, and S. Massar, High-performance photonic reservoir computer based on a coherently driven passive cavity, Optica **2**, 438 (2015).
7. F. Pedaci, S. Barland, E. Caboche, P. Genevet, M. Giudici, J. R. Tredicce, T. Ackemann, A. J. Scroggie, W. J. Firth, G.-L. Oppo, G. Tissoni, and R. Jäger, All-optical delay line using semiconductor cavity solitons, Appl. Phys. Lett. **92**, 011101 (2008).
8. C. McIntyre, A. M. Yao, G.-L. Oppo, F. Prati, and G. Tissoni, All-optical delay line based on a cavity soliton laser with injection, Phys. Rev. A **81**, 013838 (2010).
9. M. Eslami, R. Kheradmand, and F. Prati, All-optical tunable delay-line memory based on a semiconductor cavity-soliton laser, Phys. Rev. A **89**, 013818 (2014).
10. M. Eslami and R. Kheradmand, High bit-rate cavity soliton-based differential phase-shift-keying demodulator, Journal of Modern Optics **61**, 116 (2014).
11. M. Eslami, N. H. Khiavi, R. Kheradmand, F. Prati, Localized optical micromotors based on twin laser cavity solitons, Phys. Rev. A **98** , 043807 (2018).
12. Sh. R. Anbardan, M. Eslami, R. Kheradmand, and F. Prati, Cavity solitons in driven vertical-cavity-surface-emitting lasers above threshold as all-optical frequency mixers, Journal of Optics **21**, 125405 (2019).
13. Sh. R. Anbardan, M. Eslami, and R. Kheradmand, Fast and localized all-optical frequency switch based on synchronization of Cavity Solitons: A numerical study, Optics Communications **474**, 126093 (2020).
14. D. Walgraef, Spatio-Temporal Pattern Formation (Springer Verlag, Berlin, 1997).
15. N. N. Rosanov, Spatial Hysteresis and Optical Patterns (Springer, Berlin, 2002).
16. M. C. Cross and H. S. Greenside, Pattern Formation and Dynamics in Nonequilibrium Systems (Cambridge University Press, Cambridge, 2009).
17. G.-L Oppo, A. M. Yao, and D. Cuozzo, Self-organization, pattern formation, cavity solitons, and rogue waves in singly resonant optical parametric oscillators, Phys. Rev. A **88**, 043813 (2013).
18. W. J. Firth, in Soliton-Driven Photonics, edited by A. D.Boardman and A. P. Sukhorukov (Springer, Netherlands, 2001).
19. T. Ackemann and W. Firth, in Dissipative Solitons, Lecture Notes in Physics, edited by N. Akhmediev and A.Ankiewicz (Springer, Berlin, 2005).
20. M. Tlidi, M. Taki, and T. Kolokolnikov, Introduction: dissipative localized structures in extended systems, Chaos **17**, 037101 (2007).
21. T. Ackemann, W. Firth, and G.-L Oppo , Fundamentals and Applications of Spatial Dissipative Solitons in Photonic Devices, Adv. At. Mol. Opt. Phys. **57**, 323 (2009).
22. Ch.-Ch. Jeng, M.-F. Shih, K. Motzek, and Y. Kivshar, Partially incoherent optical vortices in self-focusing nonlinear media, Phys. Rev. Lett. **92**, 043904 (2004).
23. A. S. Desyatnikov, Y. S. Kivshar, and L. Torner, Optical vortices and vortex solitons, Progress in Optics Vol. 47 (North-Holland, Amsterdam, 2005), pp. 219–319.
24. P. Genevet, S. Barland, M. Giudici, and J. R. Tredicce, Bistable and addressable localized vortices in semiconductor lasers, Phys. Rev. Lett. **104** ,223902 (2010).
25. C. J. Gibson, A. M. Yao, and G.-L. Oppo, Optical rogue waves in vortex turbulence, Phys. Rev. Lett. **116**, 043903 (2016).
26. F. Selmi, S. Coulibaly, Z. Loghmari, I. Sagnes, G. Beaudoin, M. G. Clerc, S. Barbay, Spatiotemporal chaos induces extreme events in an extended microcavity Laser, Phys. Rev. Lett. **116**, 013901 (2016).
27. C. Rimoldi, S. Barland, F. Prati, and G. Tissoni, Spatiotemporal extreme events in a laser with a saturable absorber, Phys. Rev. A **95**, 023841 (2017).
28. M. Eslami, M. Khanmohammadi, R. Kheradmand, and G.-L. Oppo, Optical turbulence and transverse rogue waves in a cavity with triple-quantum-dot molecules, Phys. Rev. A **96**, 033836 (2017).
29. M. Fleischhauer, A. Imamoglu, and J. P. Marangos, Electromagnetically induced transparency: Optics in coherent media, Rev. Mod. Phys. **77**, 633 (2005).
30. G.-L. Oppo, Complex spatial structures due to atomic coherence, J. Modern Optics **57**, 1408 (2010); M. Eslami, R. Kheradmand, D. McArthur, and G.-L. Oppo, Complex structures in media displaying electromagnetically induced transparency: Pattern multistability and competition, Phys. Rev. A **90**, 023840 (2014).
31. M. Eslami, R. Kheradmand, and G.-L. Oppo, Complex structures in cavities with media displaying EIT: coexistence, defects and selection mechanism, Journal of Physics B: Atomic, Molecular and Optical Physics **53**, 075402 (2020).
32. G.-L. Oppo, Formation and control of Turing patterns and phase fronts in photonics and chemistry, Journal of Mathematical Chemistry **45**, 95 (2009).
33. T. Hansson and S. Wabnitz, Frequency comb generation beyond the Lugiato–Lefever equation: multi-stability and super cavity solitons, Journal of the Optical Society of America B **32**, 1259 (2015).
34. M. Anderson, Y. Wang, F. Leo, S. Coen, M. Erkintalo, and S. G. Murdoch, Coexistence of multiple nonlinear states in a tristable passive kerr resonator, Phys. Rev. X **7**, 031031 (2017).
35. Y.V. Kartashov, O. Alexander, and D.V. Skryabin, Multistability and coexisting soliton combs in ring resonators: the Lugiato-Lefever approach, Opt. Exp. **25**, 11550 (2017).
36. G. Slavcheva, A. V. Gorbach, A. Pimenov, A. G. Vladimirov, and D. V. Skryabin, Multi-stability and polariton solitons in microcavity wires, Opt. Lett. **40**, 1787 (2015).
37. X. Hachair, F. Pedaci, E. Caboche, S. Barland, M. Giudici, J. R. Tredicce, F. Prati, G. Tissoni, R. Kheradmand, L. A. Lugiato, I. Protsenko, and M. Brambilla, Cavity solitons in a driven VCSEL above threshold, IEEE J. Sel. Top. Quantum Electron. **12**, 339 (2006).

38. M. Eslami, R. Kheradmand, and K. M. Aghdami, Complex behavior of vertical cavity surface emitting lasers with optical injection, Phys. Scr. T **157**, 014038 (2013).
39. R. Neubecker, G.-L.Oppo, B. Thuering, and T. Tschudi, Pattern formation in a liquid-crystal light valve with feedback,including polarization, saturation, and internal threshold effects, Phys. Rev. A **52**, 791 (1995).
40. U. Bortolozzo, R. Rojas, and S. Residori, Spontaneous nucleation of localized peaks in a multistable nonlinear system, Phys. Rev. E **72**, 045201(R) (2005).
41. U. Bortolozzo, M. G. Clerc, F. Haudin, R. G. Rojas, and S. Residori, Localized States in Bi-Pattern Systems, Advances in Nonlinear Optics, Article ID 926810 (2009).
42. Ch.-Yu Hsieh, Yun-Pil Shim, M. Korkusinski, and P. Hawrylak, Physics of lateral triple quantum-dot molecules with controlled electron numbers, Rep. Prog. Phys. **75**, 114501 (2012).
43. G. Granger, L. Gaudreau, A. Kam, M. Pioro-Ladrière, S. A. Studenikin, Z. R. Wasilewski, P. Zawadzki, and A. S. Sachrajda, Three-dimensional transport diagram of a triple quantum dot, Phys. Rev. B **82**, 075304 (2010).
44. J. Roh, Y.-Sh. Park, J. Lim, and V. I. Klimov, Optically pumped colloidal-quantum-dot lasing in LED-like devices with an integrated optical cavity, Nat. Commu.**11**, 271 (2020).
45. G. Müller, M. Müller, A. Wicht, R.-H. Rinkleff, and K. Danzmann, Optical resonator with steep internal dispersion, Phys. Rev. A **56** 2385 (1997).
46. Y.-C. Liu, B.-B.Li and Y.-F. Xiao, Electromagnetically induced transparency in optical microcavities, Nanophotonics **6**, 789 (2017).
47. R. Bonifacio and L. A. Lugiato, Bistable absorption in a ring cavity, Lett. Nuovo Cim. **21**, 505 (1978).
48. L. A. Lugiato, Theory of optical bistability, in E. Wolf (ed.) Progress in Optics vol. XXI (1984).
49. A. J. Scroggie, W. J. Firth, G. S. McDonald, M. Tlidi, R. Lefever, and L. A. Lugiato, Pattern formation in a passive Kerr cavity, Chaos, Solitons & Fractals **4**, 1323 (1994).
50. D. Gomila, M. A. Matias, and P. Colet, Excitability Mediated by Localized Structures in a Dissipative Nonlinear Optical Cavity, Phys. Rev. Lett. **94**, 063905 (2005).
51. L. Lugiato, F. Prati, and M. Brambilla, Nonlinear optical systems, Cambridge University Press (2015).
52. J. M. Villas-Boas, A. O. Govorov and S. E. Ulloa, Coherent control of tunneling in a quantum dot molecule, Phys. Rev. B **69**, 125342 (2004).
53. S.-C. Tian, R.-G. Wan, C.-Z. Tong, Y.-Q Ning, L. Qin and Y. Liu, Giant Kerr nonlinearity induced by tunneling in triple quantum dot molecules, J. Opt. Soc. Am. B **31**, 1436 (2014).
54. L. V. Butov, A. Zrenner, G. Abstreiter, G. Bohm, and G. Weimann, Condensation of indirect excitons in coupled AlAs/GaAs quantum wells, Phys. Rev. Lett. **73**, 304 (1994).
55. H. Sattari, M. Sahrai, and S. Ebadollahi-Bakhtevar, Compact triple coupled quantum well system for electrical/optical control of optical bi/multistability, App. Opt. **54**, 2461 (2015).
56. H. S. Borges, L. Sanz, J. M. Villas-Boas, and A. M. Alcalde, Robust states in semiconductor quantum dot molecules, Phys. Rev. B **81**, 075322 (2010).
57. M. C. Cross and P. C. Hohenberg, Rev. Mod. Phys. **65**, 851 (1993) and forward citations.
58. G. Slavcheva, A. V. Gorbach, A. Pimenov, A. G. Vladimirov, and D. V. Skryabin, Multi-stability and polariton solitons in microcavity wires, Opt. Lett. **40**, 1787 (2015).
59. X. Hachair, L. Furfaro, J. Javaloyes, M. Giudici, S. Balle, J. Tredicce, G. Tissoni, L. A. Lugiato, M. Brambilla, and T. Maggipinto, Cavity-solitons switching in semiconductor microcavities, Phys. Rev. A **72**, 013815 (2005).
60. S. Barbay, Y. Ménesguen, X. Hachair, L. Leroy, I. Sagnes, and R. Kuszelewicz, Incoherent and coherent writing and erasure of cavity solitons in an optically pumped semiconductor amplifier, Optics Letters **31**, 1504 (2006).
61. S. Barbay and R. Kuszelewicz, Physical model for the incoherent writing/erasure of cavity solitons in semiconductor optical amplifiers, Optics Express **15**, 12457 (2007).
62. K. M. Aghdami, F. Prati, P. Caccia, G. Tissoni, L. A. Lugiato, R. Kheradmand, and H. Tajalli, Comparison of different switching techniques in a cavity soliton laser, The European Physical Journal D **47**, 447 (2008).
63. E. Taghavi, M. Eslami, and R. Kheradmand, Coherent and incoherent switching of cavity solitons in an optically injected VCSEL, Journal of Optics **21**, 015402 (2019).